Journal of Marine Research, 55, 613–631, 1997

Journal of
MARINE RESEARCH

Volume 55, Number 4

Time-dependent motions and the nonlinear bottom Ekman layer

by K. H. Brink[1]

ABSTRACT

The laminar bottom Ekman layer beneath a flow with finite relative vorticity is studied. First, the case with only a steady interior shear flow is reviewed, and then a case with a spatially uniform oscillating flow is superimposed. In both cases, the problem can be reduced to solving ordinary differential equations. The competition of two effects governs the results. The interior vorticity effectively modifies the rotation rate, but advection (especially vertically, due to Ekman pumping) tends to counteract the vorticity modification. Vertical advection keeps the time-dependent boundary layer well behaved for negative interior vorticities, but a boundary layer singularity can still exist at a single superinertial frequency when interior relative vorticity is positive.

1. Introduction

Occasionally, nature provides settings where there is both a mean flow with high relative vorticity, and relatively uniform (in space) oscillating flow. A well-studied example of this is above the summit of Fieberling Guyot, in the eastern North Pacific (Kunze and Toole, 1997; Brink, 1995). In this case, energetic K_1 diurnal tides exist above the summit, within a radius of about 5 km of the center. These tides, in turn, are an important factor in driving a laterally sheared azimuthal mean flow that approximates solid body rotation (uniform relative vorticity ω) over the summit having a mean relative vorticity of about $-0.7\,f$, where f is the Coriolis parameter. Fieberling Guyot is unlikely to be an isolated example of superimposed oscillations and a strong mean flow. Maas and van Haren (1987) for example suggest a similar feature in the North Sea. Indeed, such a combination might be reasonably common in situations where tidal rectification (e.g., Loder, 1980) is important.

1. Woods Hole Oceanographic Institution, Mail Stop 21, Woods Hole, Massachusetts, 02543-1541, U.S.A.

The steady part of the bottom Ekman layer problem with a finite interior relative vorticity was treated in a nongeophysical context by Rogers and Lance (1960), and the approach to this aspect of the problem here follows their methods closely. The effectively steady problem has also been treated in a geophysical context for the limit of small Rossby number (weak, but not vanishing relative vorticity) by Benton *et al.* (1964), Denbo and Allen (1983) and Hart (1995). It should be noted that Benton *et al.* (1964) carried out their expansions to fifth order in Rossby number, and that Hart (1995) allowed for time dependent, spatially varying interior vorticity. Further, Bennetts and Hocking (1973) considered steady flows with a finite Rossby number. The present study treats finite Rossby number flows with a spatially uniform, superimposed, oscillating flow.

2. Formulation

The problem to be solved is for horizontally unbounded, unstratified, hydrostatic conditions. The system is rotating at a constant rate about the vertical z axis and is bounded by a bottom at $z = 0$. A constant eddy viscosity, A, is assumed. In the interior, a uniform, geostrophically balanced steady shear flow plus a spatially uniform time-dependent component exist such that

$$v_0 = \omega_0 x + g(t), \tag{1a}$$

and

$$u_0 = \gamma(t), \tag{1b}$$

where (u_0, v_0) is the interior velocity, ω_0 is the (constant) interior relative vorticity, x is the coordinate perpendicular to the shear flow, ρ is the (constant) density, and p is pressure. All variations in the y directions will be ignored, except that a constant (in y) pressure gradient will be allowed.

Under these conditions, the equations of motion are

$$u_t + uu_x + wu_z - fv = -\frac{1}{\rho} p_x + Au_{zz}, \tag{2a}$$

$$v_t + uv_x + wv_z + fu = -\frac{1}{\rho} p_y + Av_{zz}, \tag{2b}$$

$$u_x + w_z = 0. \tag{2c}$$

where u and w are the velocity components in the x and z directions, respectively. Subscripts x, z and t represent partial differentiation with respect to horizontal distance, vertical distance and time, respectively. The velocity fields can be broken into two components as

$$u = \gamma(t) + \hat{u}(x, z, t), \tag{3a}$$

$$v = \omega_0 x + g(t) + \hat{v}(x, z, t) \tag{3b}$$

$$w = 0 + \hat{w}(x, z), \tag{3c}$$

and substituted into (2) to obtain

$$\hat{u}_t + \gamma_t + (\hat{u} + \gamma)\hat{u}_x + \hat{w}\hat{u}_z - f(\hat{v} + g + \omega_0 x) = -\frac{1}{\rho} p_x + A\hat{u}_{zz} \tag{4a}$$

$$\hat{v}_t + g_t + \hat{w}\hat{v}_z + (f + \omega_0 + \hat{v}_x)(\hat{u} + \gamma) = -\frac{1}{\rho} p_y + A\hat{v}_{zz}, \tag{4b}$$

$$\hat{u}_x + \hat{w}_z = 0. \tag{4c}$$

The boundary conditions are

$$\left.\begin{aligned} u &= \gamma + \hat{u} = 0 \\ v &= \hat{v} + \omega_0 x + g = 0 \\ w &= \hat{w} = 0 \end{aligned}\right\} \quad \text{at } z = 0 \tag{5a, 5b, 5c}$$

and

$$\hat{u}, \hat{v} \longrightarrow 0 \qquad \text{for } z \longrightarrow \infty \tag{5d}$$

$$\hat{w} \qquad \text{bounded for } z \longrightarrow \infty. \tag{5e}$$

The system (4) is nondimensionalized as follows

$$x = Lx', \tag{6a}$$

$$z = z^* z' = (A/f)^{1/2} z', \tag{6b}$$

$$(u, v) = V(u', v'), \tag{6c}$$

$$w = V\frac{z^*}{L} w', \tag{6d}$$

$$\omega_0 = \frac{V}{L}, \tag{6e}$$

$$(\gamma, g) = V(\gamma', g') \tag{6f}$$

$$p = (\rho LVf)p' \tag{6g}$$

$$t = f^{-1} t' \tag{6h}$$

where primes denote dimensionless quantities. Using (1) and (6), (4) becomes

$$\hat{u}_{t'} + \gamma'_{t'} + R[(\hat{u}' + \gamma')\hat{u}'_{x'} + \hat{w}'\hat{u}_{z'}] - (\hat{v}' + g' + x) = -p'_{x'} + \hat{u}'_{z'z'} \tag{7a}$$

$$\hat{v}'_{t'} + g'_{t'} + R\hat{w}'\hat{v}'_{z'} + [1 + R + R\hat{v}'_{x'}](\hat{u}' + \gamma') = -p'_{y'} + \hat{v}'_{z'z'}, \tag{7b}$$

$$\hat{u}'_{x'} + \hat{w}'_{z'} = 0, \tag{7c}$$

where the Rossby number

$$R = \frac{\omega_0}{f} \tag{8}$$

can be positive or negative depending on the sign of the shear. Henceforth, all primes on nondimensional variables will be dropped. In the interior (for large z), the boundary layer horizontal flow components ($\hat{u}$, $\hat{v}$), are expected to vanish, so the far field flows are taken to obey

$$\gamma_t - g - x = -p_x, \tag{9a}$$

$$g_t + (1 + R)\gamma = -p_y. \tag{9b}$$

This pair of equations is then subtracted from (7a, 7b) to obtain the boundary layer equations.

In order to describe the background, steady flow, time dependence will be temporarily dropped:

$$p_x = x, \tag{10a}$$

$$p_y = \gamma = g = 0. \tag{10b}$$

By assuming that

$$\hat{u} = \bar{u}(z)x, \tag{11a}$$

$$\hat{v} = \bar{v}(z)x, \tag{11b}$$

$$\hat{w} = \bar{w}(z), \tag{11c}$$

system (7) can be simplified to a set of coupled, nonlinear ordinary differential equations:

$$R(\bar{u}\,\bar{u} + \bar{w}\,\bar{u}_z) - \bar{v} = \bar{u}_{zz}, \tag{12a}$$

$$R\bar{w}\,\bar{v}_z + (1 + R + R\bar{v})\bar{u} = \bar{v}_{zz}, \tag{12b}$$

$$\bar{u} + \bar{w}_z = 0. \tag{12c}$$

The conditions (5a–c) at $z = 0$ can be restated as

$$\bar{u}(0) = 0, \tag{13a}$$

$$\bar{v}(0) = -1, \tag{13b}$$

and

$$\bar{w}(0) = 0, \tag{13c}$$

while, anticipating the boundary layer character of the flow,

$$\bar{u}, \bar{v} \to 0 \qquad z \to \infty \tag{13d}$$

$$\bar{w} \quad \text{bounded} \qquad z \to \infty. \tag{13e}$$

An analogous problem can be formulated in cylindrical coordinates with the far-field azimuthal flow in solid body rotation relative to the reference system of the boundary (Rogers and Lance, 1960). The solution to (12)–(13) is presented in Section 3.

Once the steady sheared solution is obtained, it is then possible to impose a spatially uniform, time-dependent flow, thus generalizing the oscillating Ekman layer problem (e.g., Sverdrup, 1927). Solutions are sought in the form

$$u = \bar{u}x + \gamma(t) + \tilde{u}(z, t) \tag{14a}$$

$$v = \bar{v}x + x + g(t) + \tilde{v}(z, t) \tag{14b}$$

$$w = \bar{w}, \tag{14c}$$

where the notation is as in (7), (9), (11) and where $\tilde{u}$, $\tilde{v}$ are boundary layer flows related to γ and g. Thus, at $z = 0$,

$$\tilde{u}(0, t) = -\gamma(t), \tag{15a}$$

$$\tilde{v}(0, t) = -g(t) \tag{15b}$$

and

$$\tilde{u}, \tilde{v} \to 0 \quad \text{as} \quad z \to \infty. \tag{15c}$$

Upon substitution of (14) into (7) and subtracting (9), the governing equations become

$$x\bar{u}_t + \tilde{u}_t + R[x\,\bar{u}\,\bar{u} + \tilde{u}\bar{u} + \gamma\bar{u} + x\bar{w}\,\bar{u}_z + \bar{w}\,\tilde{u}_z] - x\bar{v} - \tilde{v} = x\bar{u}_{zz} + \tilde{u}_{zz}, \tag{16a}$$

$$x\bar{v}_t + \tilde{v}_t + R\bar{w}[(x\bar{v}_z + \tilde{v}_z)] + R\gamma\bar{v} + (1 + R + R\bar{v})(x\bar{u} + \tilde{u}) = x\bar{v}_{zz} + \tilde{v}_{zz}, \tag{16b}$$

$$\bar{u} + \bar{w}_z = 0. \tag{16c}$$

Differentiating (16) with respect to x leads to equations for the sheared flow:

$$\bar{u}_t + R[\bar{u}\,\bar{u} + \bar{w}\,\bar{u}_z] - \bar{v} = \bar{u}_{zz}, \tag{17a}$$

$$\bar{v}_t + R\bar{w}\,\bar{v}_z + (1 + R + R\bar{v})\bar{u} + \bar{v}_{zz}. \tag{17b}$$

Since

$$\bar{u}(0) = 0,$$

$$\bar{v}(0) = -1,$$

and since (17) is uncoupled from the time-dependent problem, its steady solution will be identical to that of (12). The mean flow is thus unaffected by spatially uniform advection of the uniform vorticity and vertical momentum.

The governing equations for the time-dependent flow are found by subtracting (17) from (16) to obtain:

$$\tilde{u}_t + R[\overline{u}\,\tilde{u} + \overline{w}\,\tilde{u}_z] - \tilde{v} - \tilde{u}_{zz} = -R\gamma\tilde{u} \tag{18a}$$

and

$$\tilde{v}_t + R\overline{w}\,\tilde{v}_z + (1 + R + R\overline{v})\tilde{u} - \tilde{v}_{zz} = -R\gamma\tilde{v}. \tag{18b}$$

These equations are linear in $(\tilde{u}, \tilde{v})$ and show the effect of the steady flow through momentum advection and modification of the vorticity field.

3. The steady background flow

It is not obvious that (12) has any analytical solutions for $R \neq 0$, although Benton *et al.* (1964) and Denbo and Allen (1983), for example, used perturbation solutions for small R to obtain some results. Problem (12–13) was solved here by a Runge-Kutta "shooting" technique as follows. First, five equations were developed from (12) in the form

$$\overline{w}_z = \phi, \tag{19a}$$

$$\overline{v}_z = \zeta, \tag{19b}$$

$$\phi_z = \psi, \tag{19c}$$

$$\psi_z = \overline{v} + R(-\phi^2 + \overline{w}\psi), \tag{19d}$$

$$\zeta_z = R\overline{w}\zeta - (1 + R + R\overline{v})\overline{w}_z. \tag{19e}$$

Note that $\overline{u}$ is eliminated using (12c). Conditions (13a–c) provide "initial" conditions at $z = 0$, for ϕ, $\overline{v}$ and $\overline{w}$. Two other conditions, for $\overline{v}_z(= \zeta)$ and $\overline{w}_{zz}(= -\overline{u}_z = \psi)$, representing the vector bottom stress, must be found. In practice, the bottom stress magnitude

$$c = [\overline{u}_z^2(0) + \overline{v}_z^2(0)]^{1/2} \tag{20a}$$

and direction

$$\theta = -\tan^{-1}\left[\frac{\overline{u}_z(0)}{\overline{v}_z(0)}\right] \tag{20b}$$

were searched until a solution was found where $\overline{u}$ and $\overline{v}$ vanish far from the boundary, typically at $15 \leq z \leq 75$, depending on R. The numerical solutions were obtained using the Matlab© adaptive fourth and fifth order Runge-Kutta scheme "ode45" with a nominal accuracy of 10^{-8}. Isolating decaying solutions required that c and θ be found to at least seven decimal places accuracy.

Eqs. (12–13) can be used to derive relations for the Ekman transport:

$$\overline{U}_E = \int_0^\infty \overline{u}dz = -(1 + R)^{-1}\left[\overline{v}_z(0) + 2R\int_0^\infty \overline{u}\,\overline{v}\,dz\right] \tag{21a}$$

and

$$\overline{V}_E = \int_0^\infty \overline{v} dz = u_z(0) - 2R\int_0^\infty \overline{u}\,\overline{u}\, dz. \tag{21b}$$

The integrals on the right-hand sides of (21) represent the summed effects of horizontal and vertical momentum advection. A simpler form for (21a) follows from (12c) and (13):

$$\overline{U}_E = -\overline{w}(\infty). \tag{22}$$

Some insight can be gained by considering solutions far from the boundary ($z \gg 1$). In the far field, $\overline{u}$ and $\overline{v}$ become small, so the $\overline{uu}$ and $\overline{uv}$ terms in (12a) and (12b) respectively become negligible. Likewise, from (12c), $\overline{w}$ is seen to approach a constant $\overline{w}_0$. Under these assumptions, (12) can be reduced to a set of linearized equations

$$R\,\overline{w}_0\,\overline{u}_z - \overline{v} \cong \overline{u}_{zz}, \tag{23a}$$

$$R\,\overline{w}_0\,\overline{v}_z + (1 + R)\overline{u} \cong \overline{v}_{zz}. \tag{23b}$$

Solutions to this pair would have to decay for $z > 0$ and would have to match with the full nonlinear results for some large but finite elevation.

The linearized system (23) has solutions of the form

$$\overline{u} = ae^{\alpha z} \tag{24a}$$

where

$$\alpha = \eta \pm(\pm\beta^{1/2} + \eta^2)^{1/2}, \tag{24b}$$

$$\beta = -(1 + R) \tag{24c}$$

and

$$\eta = \frac{R\overline{w}_0}{2}. \tag{24d}$$

In the linear case, the two complex bounded solutions combine to form the traditional Ekman spiral. With nonlinearity and for $R > -1$, there are still two roots corresponding to oscillating, decaying behavior. The "wavelength" of the resulting spiral is determined, from (24b), by the competition of smaller $|\beta|$ making large wavelength, and more negative $R\overline{w}_0$ compressing the boundary layer thickness. In fact, for $R = -1$, the solutions reduce to

$$\alpha = 0, \qquad R\overline{w}_0 \tag{25}$$

where $R\overline{w}_0 < 0$. That is to say that a bounded, nonspiraling solution exists only because of the downward advection.

For strong negative shears, (24b) suggests rather different behavior once $\beta^{1/2}$ becomes purely real. The nonunique solutions in this range found below all have $R\overline{w}_0 < 0$, and $\overline{w}_0 =$

$O(1)$. Thus, three real, negative roots α exist, and only one positive root corresponding to unbounded growth. The transition from two degrees of freedom to three in the far-field behavior is apparently related to the loss of uniqueness. A closer inspection of (24b) suggests that no unique, decaying solutions should ever be expected for $R < -1$, i.e. for $\beta > 0$. Specifically, if $\overline{w}_0 = 0$, only oscillating, nondecaying solutions exist. If $R\overline{w}_0 < 0$, there are either three negative real roots and one positive; or 2 complex roots with negative real parts, one real negative root, and one real positive root. In either case, for $R\overline{w}_0 < 0$, there are three degrees of freedom. If $R\overline{w}_0 > 0$, only one root with a negative real part exists: apparently too few degrees of freedom. All told, it seems unlikely that a proper, unique boundary layer solution can exist for $R < -1$.

Numerical solutions to (19) were obtained in the range $-1 \leq R \leq 1$. For $R > 1$, no peculiarities appeared to be developing. For $R < -1$, however, no unique solutions could be found, e.g. for several different choices of θ, a value of c could be found that allowed the solution to decay away from the boundary.

The bottom stress magnitude c and veering angle θ are shown in Figure 1. Their variation with R is nearly linear and acts in the sense to increase the downstream bottom stress, and decrease the cross-stream stress, as R increases. The accompanying velocities, $\overline{u}$ and $\overline{v}$, are shown as profiles in Figure 2 and are contoured in Figure 3. Note that the velocities and transport do not change signs as the lateral shear, R, changes sign because the sign is accounted for in the nondimensionalization. As might be expected from the changing total vorticity in the interior, the boundary layer becomes thicker as R approaches -1 (notice, e.g., the -0.1 contour for u), but the layer thickness does not become unbounded. Rather, the transverse Ekman velocity magnitude increases as $R \rightarrow -1$, and the transverse transport magnitude (Fig. 4) also increases. [The present results differ from those of Rogers and Lance (1960) in that Figure 4 shows a monotonic decrease in transverse Ekman transport as $R \rightarrow -1$. Their results show the equivalent of a minimum at $R = -0.9$. Their minimum may be due to having the outer bound of numerical integration too small.] At the same time, as R approaches -1, the vertical wavelength of the Ekman spiral (Fig. 2 or see zero contours in Fig. 3) increases so that the spiral disappears at $R = -1$ (Fig. 5). On the other hand, for positive R, the spiral becomes more apparent, while net Ekman veering (transverse transport) decreases.

The results can be compared directly with the first order asymptotic Benton *et al.* (1964) result for transverse Ekman transport (Fig. 4). Their results yield, in the present notation

$$\overline{U}_E \cong -2^{-1/2}\left(1 - \frac{7}{20}R\right), \tag{26}$$

which compares extremely well with the present, exact, results for $|R| \lesssim 0.2$. This parameter range encompasses many oceanographic flows of interest, suggesting that in many cases, the simple result (26) may be adequate.

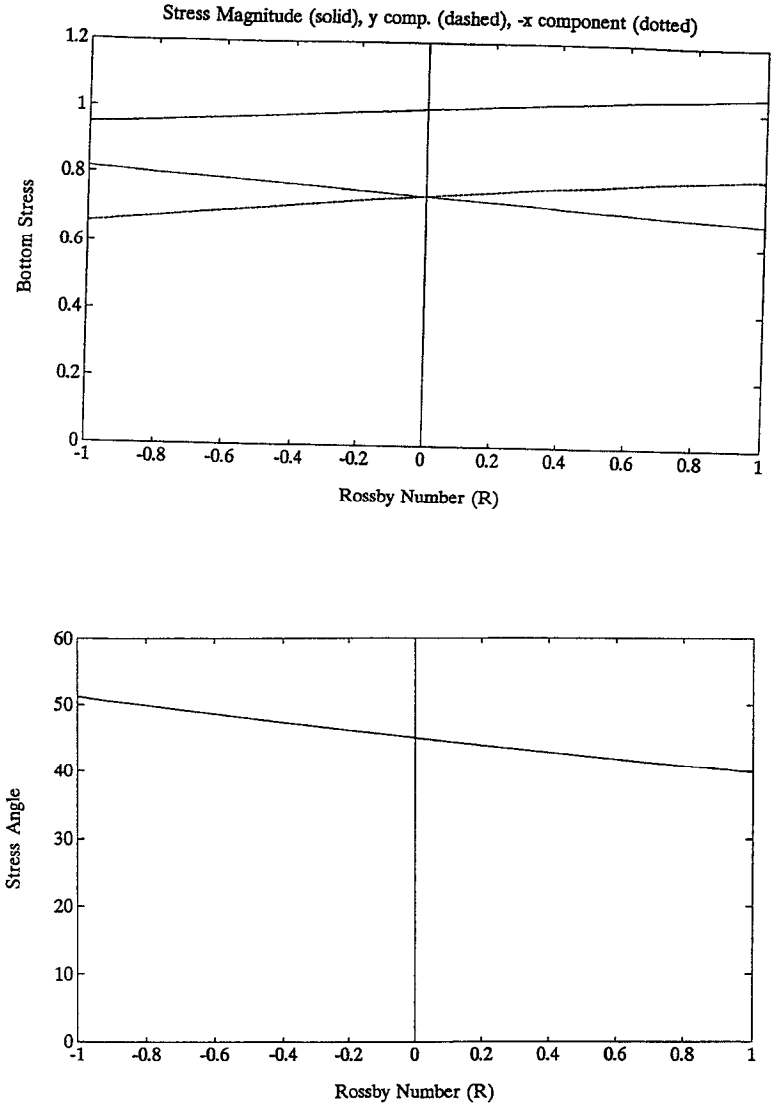

Figure 1. Upper panel: Bottom stress magnitude (solid line) versus Rossby number for the steady problem. Also shown are downstream stress (dashed line) and cross-stream stress. Lower panel: Bottom stress angle versus Rossby number.

A naive view of the problem would suggest that changes in the total interior vorticity, $(f + v_{0x})$ dimensionally, would lead to variations in the thickness of the Ekman layer (due to effectively changing the rotation rate), and to accompanying changes in the bottom stress and transverse Ekman transport. There is some qualitative truth in this concept, in that, for example, the Ekman layer becomes thinner as total vorticity increases (Fig. 3).

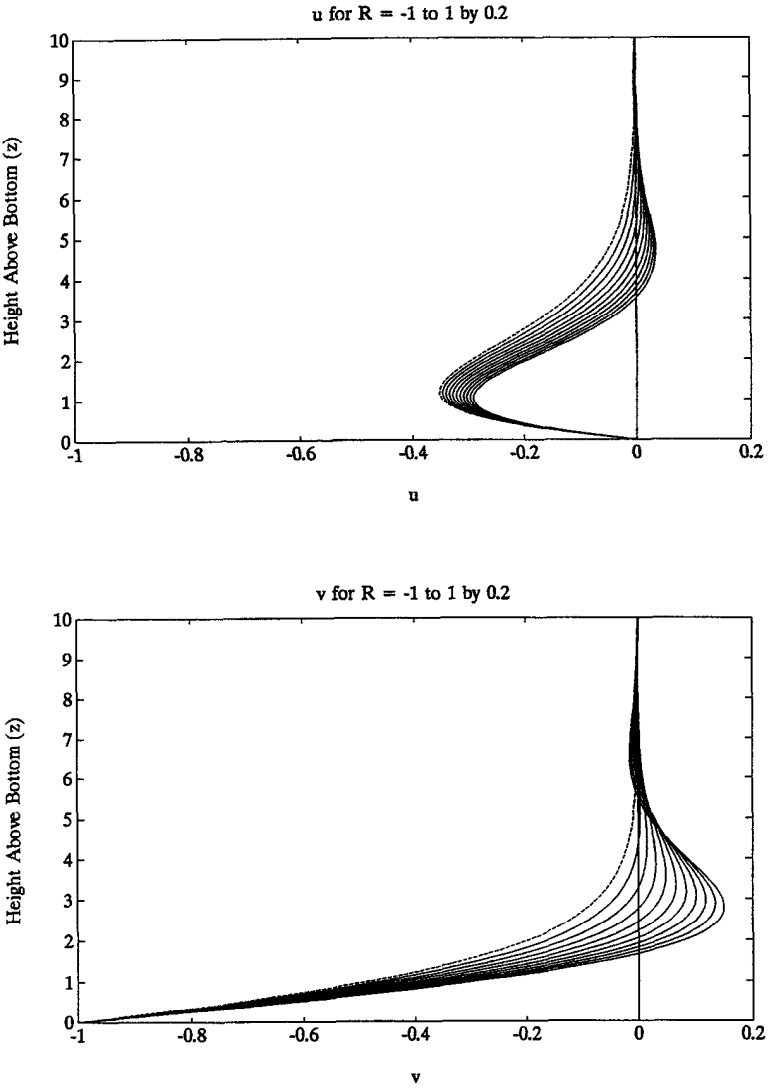

Figure 2. Profiles of boundary layer solutions for different values of R. The dashed curve is for $R = -1.0$, its nearest neighbor is for $R = -0.8$, and so forth in increments of 0.2 up to $R = 1.0$ (rightmost curve in both cases). (a) Transverse velocity. (b) Alongstream velocity.

However, the actual changes are far less than would be expected (e.g., the boundary layer does not become infinitely thick for $R = -1$) for at least two reasons. First, close enough to the boundary, all flow components approach zero, so that finite relative vorticity effects vanish close to the boundary. Second, this outlook ignores effects associated with momentum advection.

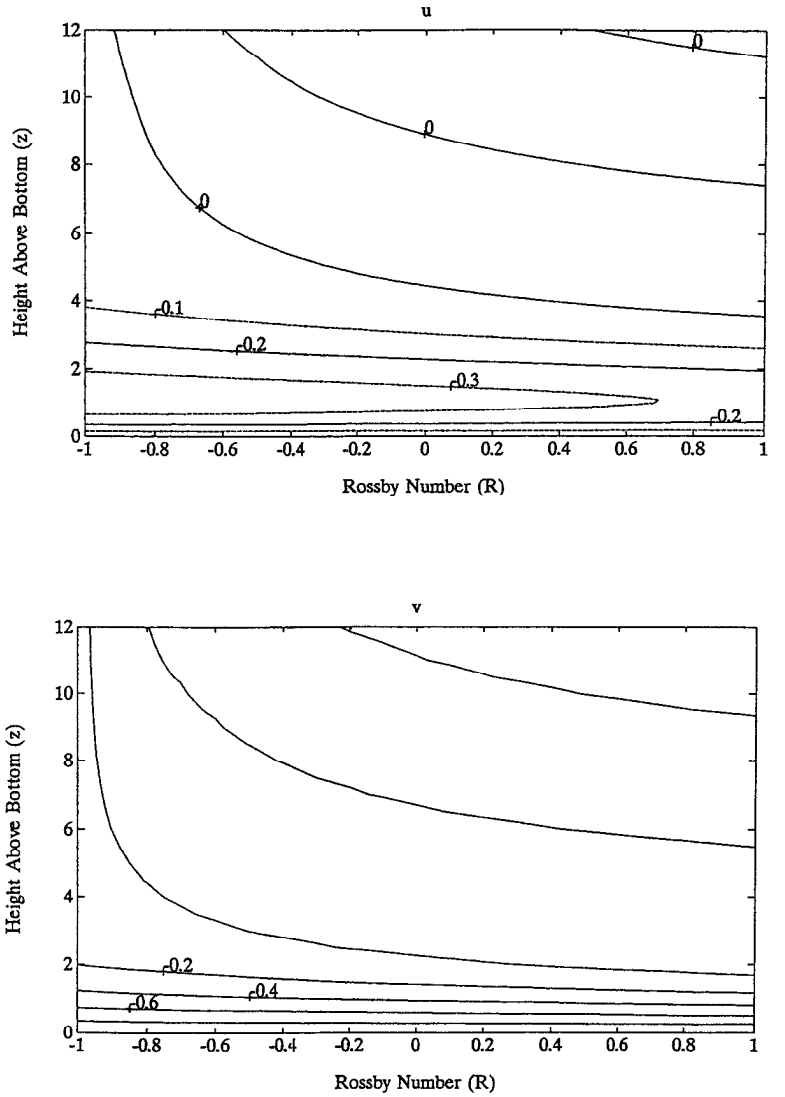

Figure 3. Contours of $\bar{u}(z)$ and $\bar{v}(z)$ as function of Rossby number for the steady problem. Dashed lines are used when the contour interval is not 0.2.

Because there is always a lateral variation in the bottom stress, the implied Ekman transport divergence requires downwelling for $R < 0$ and upwelling for $R > 0$. Thus, downward momentum advection acts to keep the boundary layer from becoming too thick for $R < 0$, and upward advection for $R > 0$ keeps the Ekman layer from becoming too thin. Similarly, the outward advection of low momentum water (Eq. 2a) for $R < 0$ acts to limit the magnitude of the transverse Ekman transport (and, of course, the opposite for $R > 0$).

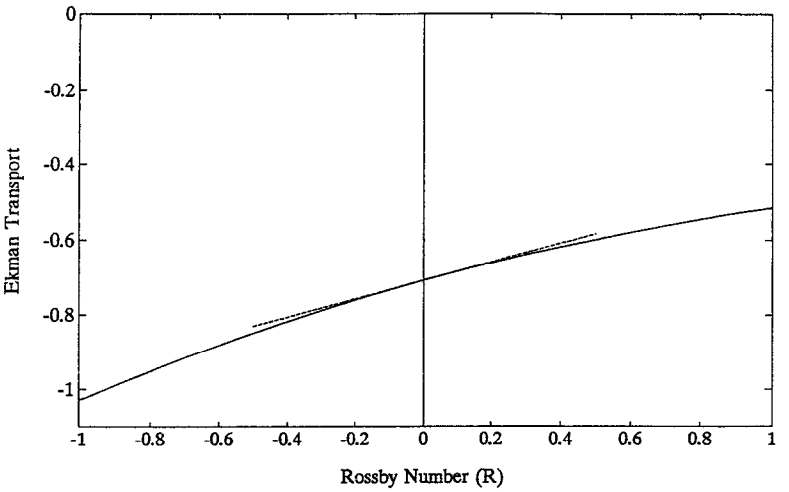

Figure 4. Transverse Ekman transport versus Rossby number for the steady problem. The dashed line represents the first order asymptotic results.

Thus, there are two competing effects introduced by nonlinearity: changed interior vorticity and momentum advection. These processes will likely come into play for any model of the bottom Ekman layer, regardless of the actual eddy viscosity used. Thus, the qualitative results obtained here (moderate changes in transport, bottom stress and layer thickness with R) should be rather general.

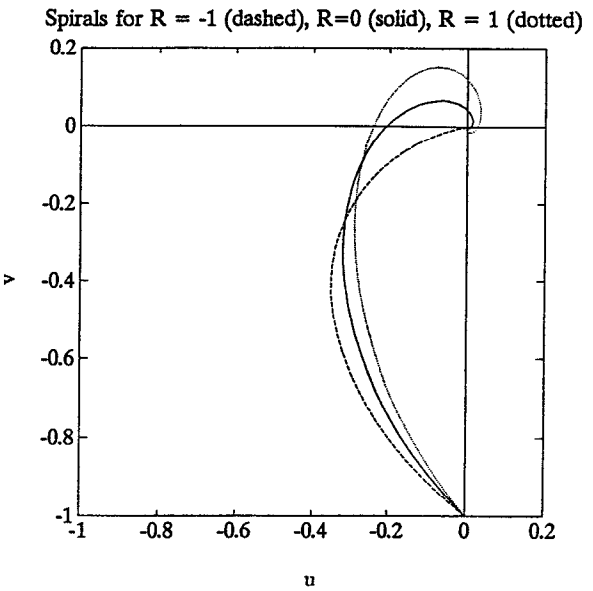

Figure 5. Steady Ekman spiral shapes for $R = -1$ (dashed), $R = 0$ (solid) and $R = 1$ (dotted).

4. Results for oscillating flow

In practice, the problem (18), (15) was solved by first assuming harmonic time dependence and $p_y = 0$:

$$g = \exp(i\sigma t), \tag{27a}$$

$$\gamma = -i\sigma(1 + R)^{-1}\exp(i\sigma t), \tag{27b}$$

$$\tilde{u} = u^*(z)\exp(i\sigma t), \tag{27c}$$

$$\tilde{v} = v^*(z)\exp(i\sigma t), \tag{27d}$$

where (27b) follows from (27a) and (9b). Note that, in this case, the interior velocity vector rotates clockwise in time. The resulting pair of ordinary differential equations is then written in finite difference form and solved numerically subject to (15) and

$$u^*(\lambda) = v^*(\lambda) = 0 \tag{28}$$

where λ is a large distance from the bottom. For the following calculations, λ was taken as 60 for $R = 0.5$ and 30 for $R = -0.5$.

Examination of the far-field behavior can again be enlightening. For large z,

$$\bar{u}, \bar{v} \to 0 \tag{29a}$$

$$\bar{w} \to w_0 \tag{29b}$$

as before. In this case, the far-field, harmonic limit of (18) becomes

$$i\sigma u^* + Rw_0 u_z^* - v^* - u_{zz}^* \cong -R\gamma\bar{u} \tag{30a}$$

and

$$i\sigma v^* + Rw_0 v_z^* + (1 + R)u^* - v_{zz}^* \cong -R\gamma\bar{v}. \tag{30b}$$

The right-hand sides are retained, as $(\bar{u}, \bar{v})$ are presumably not decaying faster than (u^*, v^*). The forcing terms on the right-hand side, however, will only tend to impose similar vertical scales to those in the steady solutions. In order to discover the natural scales of the time-dependent problem, only the homogeneous solutions to (30) will be considered. Specifically, if

$$u^* = a\exp(\alpha z) \tag{31a}$$

and

$$v^* = b\exp(\alpha z), \tag{31b}$$

the exponents are readily found to obey

$$\alpha^2 - Rw_0\alpha - i\sigma \pm [-(1 + R)]^{1/2} = 0. \tag{32}$$

Once again, vertical advection associated with Ekman pumping is seen to affect the

boundary layer thickness. Further, whereas linear, $R = 0$, time-dependent theory (e.g., Sverdrup, 1927) predicts an infinitely thick boundary layer ($\alpha = 0$) solution at the inertial frequency, here the critical frequency σ_c is shifted because of the interior vorticity, i.e.

$$\sigma_c^2 = 1 + R, \tag{33a}$$

or, dimensionally

$$\sigma_c^2 = f(f + v_{0x}). \tag{33b}$$

However, arrival at a critical frequency, in the nonlinear case, need not require an unbounded solution because of the vertical advection. Specifically, when $R < 0$, the vertical velocity is downward and two solutions to (32) with a negative real part can still exist. That is, for negative interior vorticity, the critical frequency is shifted to a subinertial value, and two of the values of α for $\sigma = \sigma_c$ will be $Rw_0(<0)$ and 0, while two are more complicated (for the example below, one of these has a negative real part). On the other hand, when interior advection is upward ($R > 0$) the critical frequency is shifted to a superinertial value and one value of α for $\sigma = \sigma_c$ is $Rw_0(>0)$, another is 0, and two are more complicated (for the example below, one of these other roots has a negative real part). That is to say that when $R > 0$, a frequency can exist where the boundary layer is infinitely thick. The importance of vertical advection to this problem thus leads to some modification of the simple concept (Maas and van Haren, 1987) of equivalance between changes in background relative vorticity and changes in Coriolis parameter (or frequency).

Solutions for the full time-dependent problem (18) were computed for a range of frequencies with $R = \pm 0.5$ and $p_y = 0$, so that fluctuating currents turn clockwise with time. Only results for $\sigma \geq 0$ are shown, as negative frequencies yielded results that were simply complex conjugates of the positive frequencies. All results are presented as total time-dependent velocity, i.e.

$$v^* + 1$$

and

$$u^* - i\sigma(1 + R)^{-1}.$$

This form accounts for the tendency for $\tilde{u}$ to vary monotonically with frequency in the interior.

For $R = -0.5$, the interior vorticity is decreased, thus making the critical frequency $\sigma_c(= 2^{-1/2})$ subinertial. Indeed, there is a tendency for the boundary layer to thicken (Fig. 6) at this frequency, but it does not become ill-behaved. For example, for $|\tilde{v} + 1|$ (Fig. 6b), the 0.9 contour is about three times as far from the bottom as when $\sigma = 0$. The unity contour reaches far from the bottom, but this is a poor indicator, given the very weak vertical gradients. The cross-stream flow (Fig. 6a) is less affected by the σ_c bulge, but does show clear Ekman veering and transport (e.g., a maximum at $z \cong 1$) for $\sigma \lesssim 0.1$. The

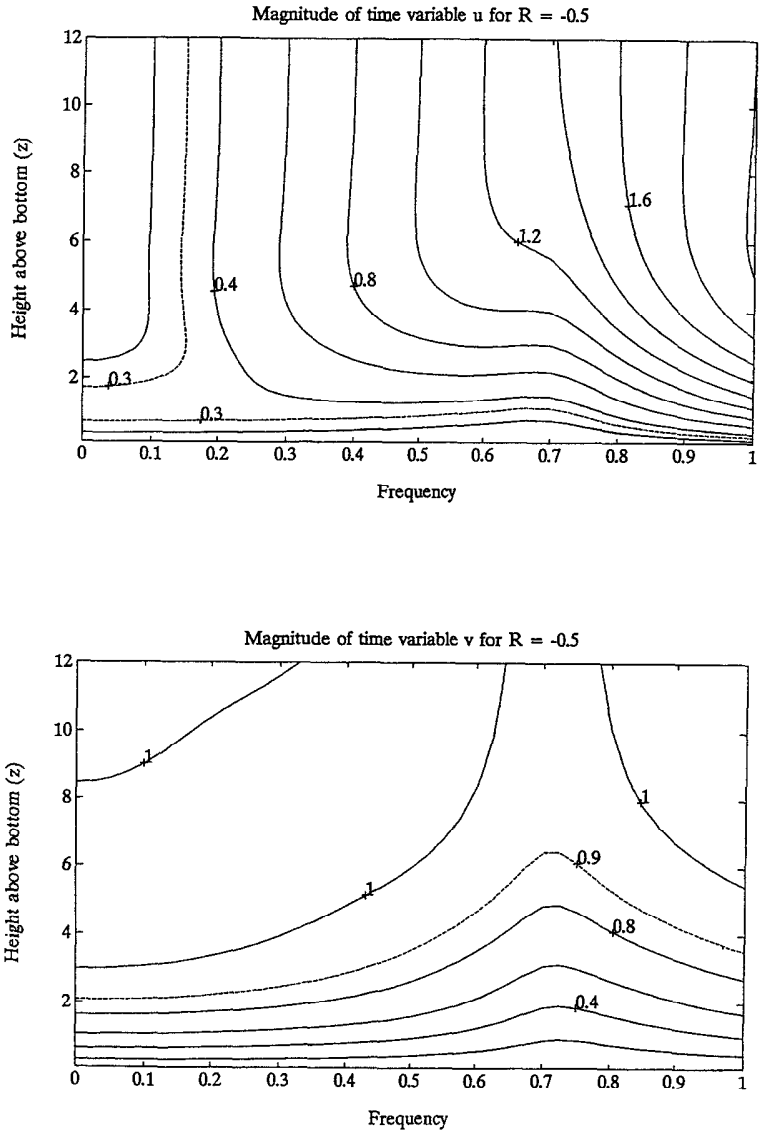

Figure 6. Contours of the magnitude of time-varying u (upper panel) and v (lower panel) for $R = -0.5$. Dashed lines are used when the contour interval is not 0.2.

phases for u and v (not shown) both indicate downward phase propagation (at least for $z \leq 12$) for $\sigma < \sigma_c$ and upward for $\sigma > \sigma_c$. Choosing appropriate values for p_x and p_y allows similar calculations for counterclockwise interior polarization, i.e., in the opposite sense of inertial oscillations. Results (not shown) are similar to those in Figure 6, but the thickening at $\sigma = \sigma_c$ is substantially less pronounced. All considered, the presence of

negative interior vorticity decreases the critical frequency and, through downward Ekman pumping, allows boundary layer solutions to exist for all frequencies.

For $R = +0.5$, the situation differs. In this case, the steady boundary layer (Fig. 3) is a good deal thinner than for $R = -0.5$. This in turn made it computationally difficult to obtain solutions for $\lambda > 30$. This limitation, combined with the tendency for a thick boundary layer near $\sigma = \sigma_c$, did not allow uniformly satisfactory solutions. Any results not deemed reliable to at least ± 0.02 have thus been masked out of the plots (Fig. 7). In this case, no proper boundary layer solution was found at $\sigma = \sigma_c = 1.5^{1/2}$, a result consistent with the existence of only one decaying far-field solution. Away from $\sigma = \sigma_c$, results are qualitatively similar to the negative vorticity ($R = -0.5$) case, except that the boundary layer tends to be thinner. Again, counterclockwise interior polarization yields similar, but less dramatic results. Phase information is similar to the case for $R = -0.5$, except that for $z \gtrsim 7$, the sense of propagation begins to alternate sign with height.

The general results of the time-dependent case are similar to those in the steady case (Section 3) in that the boundary layer tends to be thinner as R increases. The main new effect is the behavior at the critical frequencies. Negative R (decreased total interior vorticity) allows a somewhat thicker boundary layer at this frequency relative to neighboring frequencies, while positive R allows singular behavior at some superinertial frequency. It is useful to note that singular behavior is only to be found with $\sigma \geq 1$, and then only for $R \geq 0$.

It is reasonable to seek perturbation solutions for the time-dependent problem and thus determine under what circumstances the tedious numerical solutions of Section 3 (for example) can be avoided. If the steady flow is expanded in Rossby number,

$$\bar{v} = \bar{v}_0 + R\,\bar{v}_1 + R^2\bar{v}_2 + \ldots \tag{34}$$

then the governing equations for time-dependent flow (18), at lowest order, become

$$\tilde{u}_t + R[\bar{u}_0\tilde{u} + \bar{w}_0\tilde{u}_z] - \tilde{v} - \tilde{u}_{zz} = -R\gamma\bar{u}_0 \tag{35a}$$

and

$$\tilde{v}_t + R\bar{w}_0\tilde{v}_z + (1 + R + R\bar{v}_0)\tilde{u} - \tilde{v}_{zz} = -R\gamma\bar{v}_0. \tag{35b}$$

That is, the background flow is represented in terms of the strictly linear steady Ekman layer problem. It is not desirable to expand the time-dependent solution in terms of the Rossby number because then the lowest-order solution will be singular at $\sigma = \pm 1$, thus making the solution radically differ from that obtained above. Nonetheless, it is reasonable to solve (35) by the numerical approach above. Results were computed and compared with the more exact solutions in terms of the 0(1) time-dependent boundary layer transports

$$\int_0^{30} u^* dz, \qquad \int_0^{30} v^* dz.$$

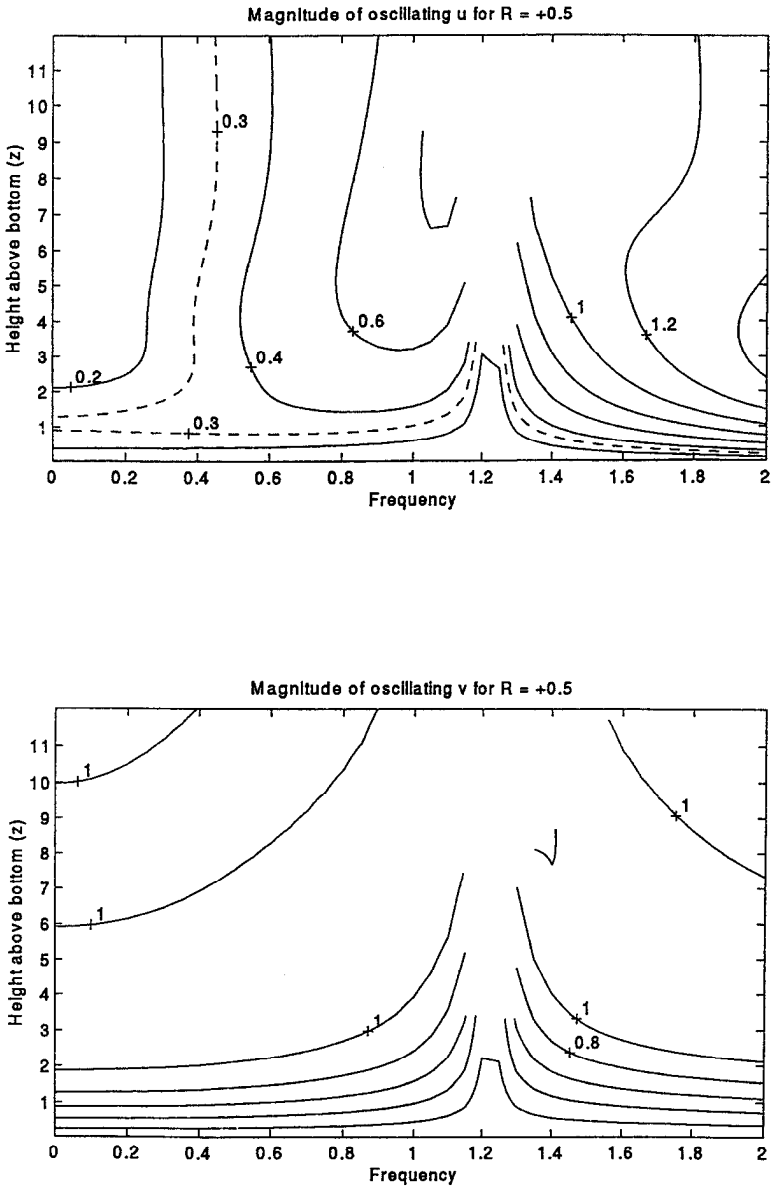

Figure 7. Contours of the magnitude of time-varying u (upper panel) and v (lower panel) for $R = +0.5$. Values not accurate to ± 0.02 have been masked. Dashed lines are used when the contour interval is not 0.2.

For $R = 0.1$, the linearized result works well over the whole frequency range $0 \leq \sigma \leq 2$: transports differ by less than 0.025, and usually much less. For larger Rossby numbers, the linearized result is only accurate for frequencies less than about $0.5\ \sigma_c$. For example, with $R = \pm 0.5$, this constraint keeps transport errors $\lesssim 0.05$. Transport errors are largest for frequencies near σ_c. In conclusion, the linearization (35) yields reasonable results for time-dependent problem at small Rossby numbers and for low frequencies at moderate Rossby numbers.

5. Conclusions

Nonlinear effects substantially affect bottom Ekman layer behavior. Changes in interior vorticity effectively modify the rotation rate, causing a tendency for the steady bottom boundary layer to thicken as the Rossby number R approaches -1. This tendency is partially compensated by momentum advection, particularly in the vertical. For example, downward advection for $R < 0$ tends to keep the boundary layer thickness finite, even when total interior vorticity vanishes. In the case of $R < -1$, the total vorticity, $1 + R + R\bar{v}$, changes sign with height above the bottom, and no unique steady solutions were found.

Time dependence is included in the form of superimposed flows that are spatially uniform far from the bottom. Nonlinear effects are similar to those in the steady problem, particularly with regard to the role of vertical advection, which assures well-behaved boundary layer properties even at the critical frequency (effective inertial frequency) as long as $-1 \leq R < 0$. For positive interior relative vorticities ($R > 0$), boundary layer singularities are obtained at a critical frequency that is always superinertial.

The key nonlinear effects in this problem are momentum advection and interior vorticity modification. Their existence should be entirely unaffected by the details of the actual eddy viscosity profile. That is to say, for example, that a positive relative vorticity immediately above the bottom Ekman layer should always lead to upward Ekman pumping. Stratification could have some substantial effects through the inhibition of interior vertical velocities, but this effect ought to be negligible as long as the vertical scale of the interior flow is larger than the boundary layer thickness. Over a sloping bottom with stratification, e.g., Trowbridge and Lentz (1991), the actual nature of the bottom boundary layer changes, so that it is unclear how the present results will apply.

Acknowledgments. This work was supported by the Office of Naval Research, Physical Oceanography code through grant N00014-94-1-0226. Comments and discussions with Alan Faller, Eric Kunze, Steve Lentz, George Veronis and an anonymous reviewer were all very helpful. This is WHOI contribution no. 9201.

REFERENCES

Bennetts, D. A. and L. M. Hocking. 1973. On nonlinear Ekman and Stewartson layers in a rotating fluid. Proc. Roy. Soc. London, A, *333,* 469–489.

Benton, G. S., F. B. Lipps and S.-Y. Tuann. 1964. The structure of the Ekman layer for geostrophic flows with lateral shear. Tellus, *XVI,* 186–199.

Brink, K. H. 1995. Tidal and lower frequency currents above Fieberling Guyot. J. Geophys. Res., *100*(C6), 10,817–10,832.

Denbo, D. W. and J. S. Allen. 1983. Mean flow generation on a continental margin by periodic wind forcing. J. Phys. Oceanogr., *13,* 78–92.

Hart, J. E. 1995. Nonlinear Ekman suction and ageostrophic effects in rapidly rotating flows. Geophys. Astrophys. Fluid Dyn., *79,* 201–222.

Kunze, E. and J. M. Toole. 1997. Fine- and microstructure observations of trapped diurnal oscillations atop Fieberling Seamount. J. Phys. Oceanogr., (in press).

Loder, J. H. 1980. Topographic rectification on the sides of Georges Bank. J. Phys. Oceanogr., *10,* 1399–1416.

Maas, L. R. M. and J. J. M. van Haren. 1987. Observations on the vertical structure of tidal and inertial currents in the central North Sea. J. Mar. Res., *45,* 293–318.

Rogers, M. H. and G. N. Lance. 1960. The rotationally symmetric flow of a viscous fluid in the presence of an infinite rotating disk. J. Fluid Mech., *7,* 617–631.

Sverdrup, H. V. 1927. Dynamics of tides on the North Siberian Shelf. Geof. Publik., *4,* 3–75.

Trowbridge, J. H. and S. J. Lentz. 1991. Asymmetric behavior of an oceanic boundary layer above a sloping bottom. J. Phys. Oceanogr., *21,* 1171–1185.

Received: *14 March, 1996;* revised: *7 March, 1997.*